

WHOI Proceedings 2024

Oceanic internal tides: do they get phased at the Equator?

Camille Moisset, Bruce Sutherland, Lois Baker

December 11, 2025

1 Introduction

Oceanic tides are an essential component of the global ocean circulation, with an important role in the exchanges between the different energy reservoirs [15, 2]. However, two different contributions need to be separated: the first is the barotropic tide, generated by astronomical forcing, which produces a large scale movement of water masses across the entire global ocean; the second is baroclinic tide (or internal tide) which are internal waves excited by the movement of the water masses over topography [e.g. 6, 5]. These waves then propagate away from their sources as low vertical modes and interact with numerous other oceanic processes [e.g. 4]. The dynamics of internal tides is incredibly rich involving complex generation mechanisms, their interactions with topography, but also wave-wave and wave-mean flow interactions, all through the stratified and rotating fluid that is the ocean [see 10, 14, 13, for reviews on different dynamical aspects]. Internal tides are a significant source for deep oceanic mixing through their non-linear dynamics that ultimately induce turbulent dissipation and diapycnal mixing.

The lunar semidiurnal internal tide, denoted M2, is the most energetic tidal mode excited in Earth oceans and, as such, a major actor of oceanic dynamics. It is excited at a fixed frequency $\omega_0 = 1.4 \times 10^{-4} \text{ rad.s}^{-1}$ and propagates over long distances as low modes with a horizontal wavelength around 150 kilometers [e.g. 3, 18]. The ultimate fate of the baroclinic tides remains uncertain but a significant number of processes are proposed, amongst them non-linear breaking, triadic interactions, scattering of the energy to higher modes, and interaction with currents and eddies. Likewise, the interaction between the internal tides and eddy fields could cause such incoherences in the tidal signal [16]. It is also possible that strong currents and shelf fronts influence the dynamics of the M2 internal tide [9].

Satellite altimetry provides a way to track the baroclinic tidal signal over the global ocean, as oscillations of the interior affect the surface of the ocean. But in the region of the Equatorial Pacific, such observations show that the M2 signal (for example propagating northward from its generation near the French Polynesia Islands) seems to disappear when the internal waves cross the Equator (see fig. 1 from [1]). Buijsman et al. [1] argue that it could be due to a loss of coherence of the M2 signal and they hinted that equatorial jets (see figure 1) could play a significant role: the vertical and meridional variations in the

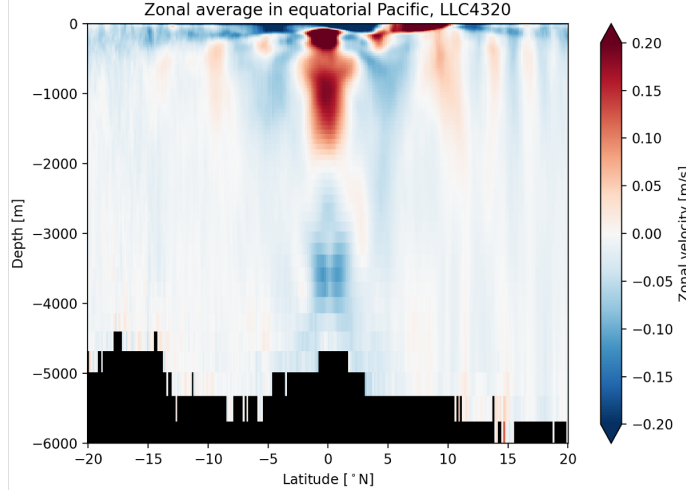


Figure 1: Vertical structure of the zonal equatorial current, computed using the LLC4320 configuration of the Massachusetts Institute of Technology general circulation model (MIT-gcm, [19])

zonal currents and the stratification can scatter the energy to higher modes and modify the phase and group speed of internal waves resulting in their incoherences. In such type of observations, the signal of the M2 internal tide is extracted using a harmonic fit to the excitation frequency of the tidal mode, meaning that incoherences could induce a significant loss of information.

We investigate whether the dynamics of the wave-mean flow interaction between the M2 internal wave and the equatorial jets could cause a loss of coherence in the M2 altimetry signal. To do so, we study the more general interaction between a vertical mode 1 internal tide wavepacket and a vertically sheared zonal jet. We follow the work of Kelly et al. [7, 8, 12] who proposed a model able to decompose the modal dynamics of the M2 internal tides. In particular, linear wave-mean flow interactions are retained but non-linear wave-wave interactions are neglected. Section 2 details the formalism of the vertical mode decomposition for internal tides, as well as the analytical framework used in our model. Simulations are realised using Dedalus [17], the numerical setup and parameters which are presented in section 3. Section 4 show the results for a simplified model in which the ocean is supposed to linearly stratified. This approximation allows for the exact comparison between the analytic calculations and the simulations. The conclusions and perspectives for future work are presented in section 5.

2 Analytical framework

2.1 General equations

We use the tangent plane approximation to describe a patch of the Equatorial Pacific Ocean as a Cartesian box, where (x, y, z) represent longitude, latitude and depth respectively,

with unit vectors $(\mathbf{e}_x, \mathbf{e}_y, \mathbf{e}_z)$. We consider the fully non-linear Euler equations with the Boussinesq approximation:

$$\partial_t \mathbf{u}_T + (\mathbf{u}_T \cdot \nabla) \mathbf{u}_T + \mathbf{f} \times \mathbf{u}_T = -\nabla p + b_T \mathbf{e}_z, \quad (1a)$$

$$\partial_t b_T + \mathbf{u}_T \cdot \nabla b_T = 0, \quad (1b)$$

$$\nabla \cdot \mathbf{u}_T = 0, \quad (1c)$$

where $\mathbf{u}_T = (u_T, v_T, w_T) = (U + u, v, w)$ is the total velocity field (including currents and waves, with U the velocity of the current), $\mathbf{f} = 2\boldsymbol{\Omega}_0 \sin \lambda$ the Coriolis parameter with $\boldsymbol{\Omega}_0$ the rotation vector and λ the latitude. $p = P/\rho_0$ is the reduced pressure where P is the dynamic pressure, the density has been decomposed as $\rho = \rho_0 + \bar{\rho}(z) + \rho(x, y, z, t)$ with ρ_0 a reference density, $\bar{\rho}$ the mean density profile and ρ the perturbation density. The squared buoyancy frequency is $\bar{N}^2 = -g\bar{\rho}'/\rho_0 = -\bar{b}'$, where g is gravity and the primes denote derivatives. The total buoyancy field is $b_T = B + \bar{b} + b$ with B the buoyancy perturbation corresponding to the zonal current, \bar{b} that of the background stratification and b that of the waves.

At the Equator, in the f -plane approximation the traditional Coriolis parameter $\mathbf{f} = (0, 0, f)$ goes to zero so we use the β -plane approximation $f = \beta y$ (with constant $\beta = 2 \times 10^{-11} \text{ m}^{-1} \text{ s}^{-1}$).

The mean flow U and its associated buoyancy B and pressure fields P_U verify the geostrophic and hydrostatic balance:

$$\beta y U = -\partial_y P_U, \quad (2a)$$

$$0 = -\partial_z P_U + B, \quad (2b)$$

which leads to

$$\partial_y B = -\beta y \partial_z U. \quad (3)$$

2.2 Base state

The base velocity considered is a zonal jet with separated meridional and vertical dependencies:

$$\mathbf{U} = (U(y, z), 0, 0) \quad \text{with} \quad U(y, z) = E(y) \tilde{U}(z), \quad (4)$$

where the meridional structure $E(y)$ is taken as a Gaussian:

$$E(y) = \exp\left(-\frac{y^2}{2W^2}\right), \quad (5)$$

with the characteristic width of the jet denoted by W .

In what follows, $\tilde{U}(z)$ will be either a constant or a cosine function and \bar{N}^2 will be a constant. It is however possible to generalise to more complex and realistic jet configurations and background stratification.

Using (3), the associated base buoyancy is in hydrostatic and equatorial geostrophic balance:

$$B(y, z) = \beta W^2 E(y) \tilde{U}'(z). \quad (6)$$

The background stratification includes the contribution of the Equatorial jet ($\partial_z B$) and the far field stratification:

$$N^2(y, z) = \beta W^2 E(y) \tilde{U}''(z) + \bar{N}^2(z). \quad (7)$$

2.3 Equations for the perturbations

The base state (4-6) is subjected to perturbation by the internal tide. The total fields are given by:

$$(u_T, v_T, w_T, p_T, b_T) = (U, 0, 0, P_U, B) + (u, v, w, p, b). \quad (8)$$

Substituting and neglecting non-linear wave-wave interaction terms in (1) yields the linearized system for the evolution of waves:

$$\partial_t u + E \tilde{U} \partial_x u + E' \tilde{U} v + E \tilde{U}' w - \beta y v = -\partial_x p, \quad (9a)$$

$$\partial_t v + E \tilde{U} \partial_x v + \beta y u = -\partial_y p, \quad (9b)$$

$$\alpha \left(\partial_t w + E \tilde{U} \partial_x w \right) = -\partial_z p + b, \quad (9c)$$

$$\partial_t b + E \tilde{U} \partial_x b + E' \tilde{U}' \beta W^2 v + \beta W^2 E \tilde{U}'' w + \bar{N}^2 w = 0, \quad (9d)$$

$$\partial_x u + \partial_y v + \partial_z w = 0 \quad (9e)$$

where $\alpha \in \{0, 1\}$ allows to distinguish between the hydrostatic approximation ($\alpha = 0$) and non-hydrostatic case ($\alpha = 1$).

2.4 Vertical mode decomposition for internal tides

We will consider internal tides incident upon and interacting with equatorial jets. They are initialised far from the equator, where the equatorial currents are negligibly small. Here we describe the process of determining the internal structure of these waves.

2.4.1 General formalism

We derive the vertical structure of internal tides with no background flow ($U = 0$). Hydrostatic balance is also assumed by setting α to zero. The system (9) is linear and we expand the perturbations using the plane wave ansatz:

$$(u, v, w, p, b)(x, y, z, t) = (\hat{u}, \hat{v}, \hat{w}, \hat{p}, \hat{b})(z) e^{i(k_x x + k_y y - \omega t)}, \quad (10)$$

where k_x and k_y are the wavenumbers in the zonal and meridional directions respectively and ω is the frequency. The system (9) becomes:

$$-i\omega \hat{u} - \beta y_0 \hat{v} = -ik_x \hat{p}, \quad (11a)$$

$$-i\omega \hat{v} + \beta y_0 \hat{u} = -ik_y \hat{p}, \quad (11b)$$

$$0 = -\hat{p}' + \hat{b}, \quad (11c)$$

$$-i\omega \hat{b} + \bar{N}^2 \hat{w} = 0, \quad (11d)$$

$$ik_x \hat{u} + ik_y \hat{v} + \hat{w}' = 0, \quad (11e)$$

in which y_0 is the initial latitude of the waves with $|y_0| \gg W$. The system (11) reduces to:

$$\hat{w}'' + k_h^2 \frac{\overline{N}^2(z)}{\omega^2 - (\beta y_0)^2} \hat{w} = 0, \quad (12)$$

where $k_h^2 = k_x^2 + k_y^2$.

The solution of (12) gives a sum of vertical modes $\hat{w} = \sum_n w_n \Phi_n(z)$ where the Φ_n satisfy the Sturm-Liouville problem:

$$\Phi_n'' + \frac{\overline{N}^2(z)}{c_n^2} \Phi_n = 0 \quad \text{with} \quad \Phi_n(0) = \Phi_n(-H) = 0, \quad (13)$$

with $c_n^2 = (\omega^2 - (\beta y_0)^2)/k_h^2$ as the eigenvalue and H the height of the domain. This gives the dispersion relation $\omega^2 = c_n^2 k_h^2 + (\beta y_0)^2$. The vertical modes, Φ_n , are orthogonal with respect to the weight function $\overline{N}^2(z)$. The normalisation is chosen so that $\max(|\Phi_n|) = 1$. Using (11) we can derive the corresponding expressions for horizontal velocity, pressure and buoyancy as a sum of vertical modes:

$$[\hat{u}, \hat{v}, \hat{p}](z) = \sum_{n=0}^{\infty} [u_n, v_n, p_n] \phi_n(z), \quad (14a)$$

$$\hat{b}(z) = \sum_{n=0}^{\infty} b_n \overline{N}^2(z) \Phi_n(z) \quad (14b)$$

where $\phi_n = \Phi_n'$.

2.4.2 Case $\overline{N} = \text{constant}$

In the case where $\overline{N} = \overline{N}_0 = \text{constant}$, equation (13) reduces to that of a harmonic oscillator:

$$\Phi_n'' + m_n^2 \Phi_n = 0 \quad \text{with} \quad m_n^2 = \frac{\overline{N}_0^2}{\omega^2 - (\beta y_0)^2} k_h^2. \quad (15)$$

Combined with the boundary conditions (13), the vertical structure functions Φ_n can be expanded as a series of sine functions:

$$\Phi_n(z) = \sin(m_n z), \quad (16)$$

where $m_n = n\pi/H$, $n = 1, 2, \dots$

Likewise,

$$\phi_n(z) = m_n \cos(m_n z). \quad (17)$$

Figure (2) shows the first three vertical structure functions for the case $\overline{N}_0^2 = 1 \times 10^{-4} \text{ s}^{-2}$, with $H = 5000 \text{ m}$.

From (15), the dispersion relation is given by

$$\omega^2 = \overline{N}_0^2 \left(\frac{k_h}{m_n} \right)^2 + (\beta y_0)^2. \quad (18)$$

Thus, specifying the frequency ω and mode number n of the initial waves gives the corresponding magnitude of the horizontal wavenumber k_h .

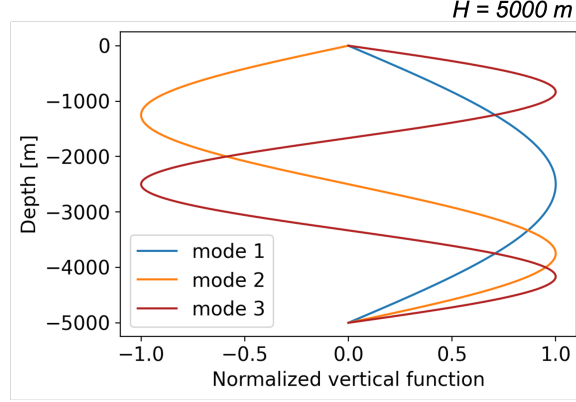


Figure 2: Three first vertical structure functions, Φ_n , for $\overline{N_0^2} = 1 \times 10^{-4} \text{ s}^{-2}$ and $H = 5000 \text{ m}$.

2.5 Ray tracing theory

Ray tracing predicts the path of the wave energy, as it moves at the group velocity \mathbf{c}_g . For horizontal motion:

$$\mathbf{c}_g = \nabla_{\mathbf{k}} \omega = \left(\frac{\partial \omega}{\partial k_x}, \frac{\partial \omega}{\partial k_y} \right) \quad (19)$$

This is different from the phase velocity \mathbf{c}_p that gives the velocity of the crests:

$$\mathbf{c}_p = \left(\frac{\omega}{|\mathbf{k}|} \right) \hat{\mathbf{k}} = \frac{\mathbf{k}}{|\mathbf{k}|^2} \omega, \quad (20)$$

In the long wave limit to be considered here, the group and phase velocity are in the same direction.

The addition of a mean flow $\mathbf{U} = U(y, z)\mathbf{e}_x$ will introduce a difference between the absolute frequency ω_0 and the intrinsic frequency ω_{int} , that are linked through:

$$\omega_0 = \omega_{\text{int}} + U k_x, \quad (21)$$

where $\omega_0 = 1.4 \times 10^{-4} \text{ rad.s}^{-1}$ is the excitation frequency of the M2 internal tide and ω_{int} the intrinsic frequency satisfies the dispersion relation for waves in stationary fluid. In all the expressions of sections 2.4.1 and 2.4.2 we replace $\omega \rightarrow \omega_{\text{int}}$.

In the absence of mean flow, (21) reduces to:

$$\omega_0 = \omega_{\text{int}}, \quad (22)$$

and ω_0 verifies the dispersion relation and all the results of sections 2.4.1 and 2.4.2.

As waves move inside the equatorial jet, it is necessary to separate:

- the absolute frequency ω_0 , which is the frequency observed from the fixed frame: it is composed of the intrinsic frequency ω_{int} and a Doppler-shift that arise from the movement of the background fluid U ;

- the intrinsic frequency ω_{int} , which is the frequency that corresponds to the frame moving with the mean-flow.

The separation between ω_0 and ω_{int} induced by the presence of the mean flow is inherited by the group velocity (19), such that:

$$c_{gx_0} = c_{gx_{\text{int}}} + U, \quad c_{gy_0} = c_{gy_{\text{int}}} \quad (23)$$

where $(c_{gx_{\text{int}}}, c_{gy_{\text{int}}})$ are given by injecting the dispersion relation (18) in equation (19).

For ray tracing to be valid outside and inside of the jet, the vertical and horizontal scale of variations of the waves must be much shorter than the characteristic scale of background variations of N and U respectively. The ray tracing equations yield the evolution of the position of the wavepacket (x, y) and its direction (k_x, k_y) :

$$\frac{dx}{dt} = \frac{\partial \omega_0}{\partial k_x} = c_{gx_{\text{int}}} + U, \quad \frac{dk_x}{dt} = -\frac{\partial \omega_0}{\partial x}, \quad (24a)$$

$$\frac{dy}{dt} = \frac{\partial \omega_0}{\partial k_y} = c_{gy_{\text{int}}}, \quad \frac{dk_y}{dt} = -\frac{\partial \omega_0}{\partial y}. \quad (24b)$$

For both cases (21) or (22), the dispersion relation yields:

$$\omega = \omega(k_x, k_y; y) = \omega_{\text{int}} + U k_x, \quad \omega_{\text{int}} = c_n^2 k_h^2 + (\beta y)^2. \quad (25)$$

which, combined with the right-equation of (24a) gives

$$k_x = k_{x_0} = \text{constant}. \quad (26)$$

The left hand equations of (24), gives the slope in the horizontal of the path:

$$\frac{dx}{dy} = \frac{c_{gx_{\text{int}}} + U}{c_{gy_{\text{int}}}} \quad (27)$$

Given the dispersion relation (25), k_y is implicitly a function of y , likewise $c_{gx} = \partial \omega_0 / \partial k_x$ and $c_{gy} = \partial \omega_0 / \partial k_y$ are implicitly functions of y .

If $U = E(y)$, independent of z , then (27) can be integrated to give the path starting at (x_0, y_0) :

$$x(y) = \int_{y_0}^y \frac{c_{gx_{\text{int}}}(\tilde{y}) + E(\tilde{y})}{c_{gy_{\text{int}}}(\tilde{y})} d\tilde{y} + x_0 \quad (28)$$

Ray tracing helps reveal how the β -plane and jet influence the dynamics of the wavepacket.

For example, ignoring the β -effect and supposing $U = E(y)$, (24b) yields

$$\frac{dk_y}{dt} = -k_{x_0} E'(y). \quad (29)$$

Figure 3 shows how the results from this translate to wave dynamics. Variations of U change k_y affecting the wavelength and orientation of the wavepacket. If $E' > 0$, then k_y decreases. The wavepacket would contract and deviate away from northward (figure 3, bottom right). Ultimately, this could lead to total reflection. Conversely, if $E' < 0$ and k_y increases, the wavepacket would redirect more toward the north where $k_y \rightarrow \infty$ (figure 3, top panel) and this could encounter critical layers.

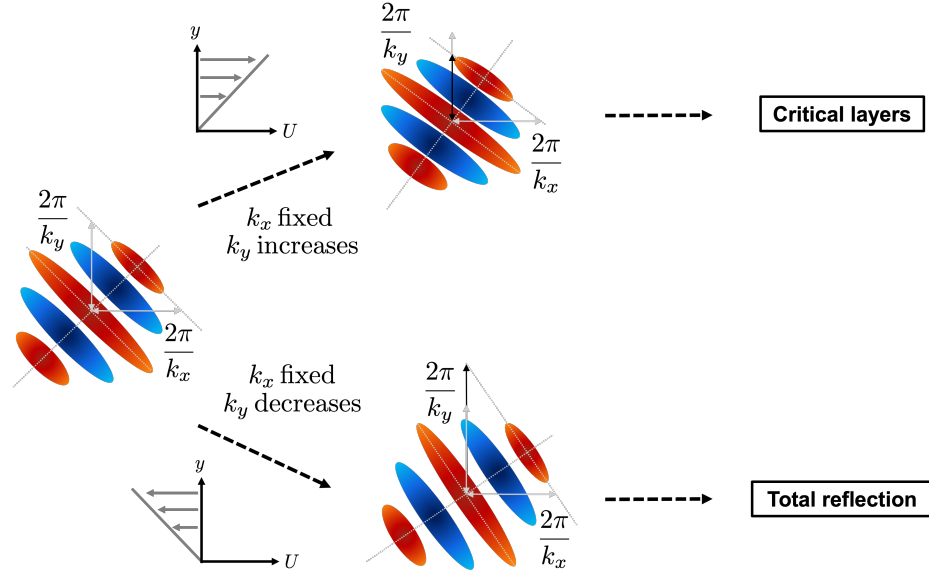


Figure 3: Schematics of the evolution of the wavepacket when interacting with a uniform jet ignoring the β effect. Initial situation is displayed in the center, with wavenumbers drawn in grey arrows. In the upper part, the wavepacket is incident upon a positive horizontal shear so that k_y increases while k_x stays fixed (black arrows), ultimately reacting to a critical layer where $k_y \rightarrow \infty$. In the lower part, the wavepacket is incident upon a negative horizontal shear and k_y decreases while k_x stays fixed (black arrows), ultimately leading to a total reflection of the wavepacket where $k_y \rightarrow 0$.

2.6 Modal wave equations

The modal wave equations are obtained by substituting the expansions (14) into the general equations (9). Multiplying (9a), (9b) and (9e) by ϕ_n , and (9c) and (9d) by Φ_n and integrating in the vertical, orthogonality allows us to extract the equations for the evolution of the amplitudes of each mode. Equation (9c) gives

$$0 = p_n + c_n^2 b_n, \quad (30)$$

and equation (9e) gives

$$\partial_x u_n + \partial_y v_n + w_n = 0. \quad (31)$$

These diagnostic equations are used to replace w_n and p_n in the remaining equations for horizontal velocity and buoyancy. From (9a):

$$\partial_t u_n + \sum_{m=0}^{\infty} (E \partial_x u_m C_{1nm} + v_m E' C_{1nm} + E'(y) w_m C_{2nm}) - \beta y v_n - c_n^2 \partial_x b_n = 0, \quad (32)$$

where the interaction coefficients between the vertical structure of the modes and the vertical structure of the jet are given by

$$C_{1nm} = \frac{\int_{-H}^0 \tilde{U} \Phi'_n \Phi'_m dz}{\int_{-H}^0 (\Phi'_n)^2 dz} \quad \text{and} \quad C_{2nm} = \frac{\int_{-H}^0 \tilde{U}' \Phi'_n \Phi'_m dz}{\int_{-H}^0 (\Phi'_n)^2 dz}. \quad (33)$$

From (9b), we find

$$\partial_t v_n + \sum_{m=0}^{\infty} (E \partial_x v_m C_{1nm}) + \beta y u_n - c_n^2 \partial_y b_n = 0, \quad (34)$$

and from (9d),

$$\partial_t b_n + \sum_{m=0}^{\infty} [E \partial_x b_m C_{3nm} + \beta W^2 E' v_m C_{4nm} - \beta W^2 E (\partial_x u_m + \partial_y v_m) C_{5nm}] - (\partial_x u_n + \partial_y v_n) = 0, \quad (35)$$

in which

$$C_{3nm} = \frac{\int_{-H}^0 \bar{N}^2 \tilde{U} \Phi_n \Phi_m dz}{\int_{-H}^0 \bar{N}^2 \Phi_n^2 dz}, \quad C_{4nm} = \frac{\int_{-H}^0 \bar{N}^2 \tilde{U}' \Phi'_n \Phi'_m dz}{\int_{-H}^0 \bar{N}^2 \Phi_n^2 dz}, \quad \text{and} \quad C_{5nm} = \frac{\int_{-H}^0 \tilde{U}'' \Phi_n \Phi_m dz}{\int_{-H}^0 \bar{N}^2 \Phi_n^2 dz}. \quad (36)$$

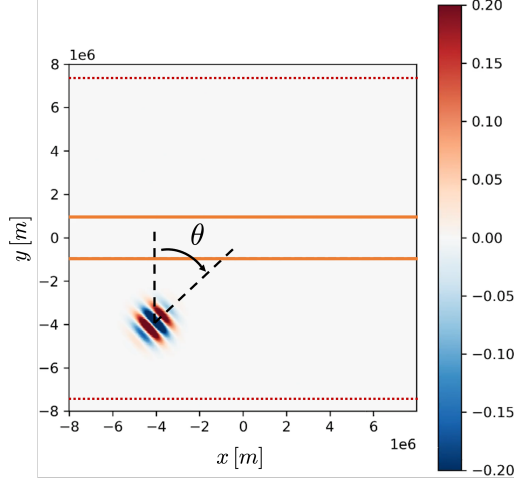


Figure 4: Initial condition in a typical simulation: the wavepacket is launched from the position (x_0, y_0) in the southern hemisphere at an angle θ from north. Jet limits at $y \pm 2W$ are shown by orange lines, sponge layers limits are shown by red dashed lines.

3 Numerical methods

The equations for the mode amplitude evolution (32), (34) and (35) are solved using Dedalus [17]. The coefficients (33) and (36) are solved beforehand, using vertical modes Φ_n computed with the Galerkin method for a given stratification profile from (13), and a prescribed vertical profile \tilde{U} for the jet.

The domain represents a patch of the Equatorial Pacific latitudinally centered on the equator. The domain is such that $x \in [-L_x; L_x]$ and $y \in [-L_y; L_y]$ where $(L_x, L_y) = (8000, 8000)$ km (figure (4)). It needs to be sufficiently large to allow the wavepacket to propagate toward the jet, interact with it and exit on the other side. The equator, specifically, is centered at $y = 0$. The equatorial jet uniformly spans the zonal direction. It is centered on the equator with an horizontal width of $W=400$ km. The domain is periodic in both x and y with zonally uniform sponge layers located near the north and south boundaries of the domain to prevent the waves crossing the top and bottom boundaries.

The resolution is set to $(N_x, N_y) = (512, 512)$ so that the wavelength of the internal tides are resolved by at least 16 grid points. The typical simulation duration is approximately 8.7 days: the number of iterations is fixed at 1500 with a timestep of $dt = 500$ s ensuring numerical stability of the CFL criterion. Viscosity is also added for numerical stability. It is fixed at $\nu = 1 \text{ m}^2 \cdot \text{s}^{-1}$, though much larger than the viscosity of sea water, it is still small enough that dissipation of the waves is insignificant.

The dimensions of the domain are chosen to match the physics of the problem: the M2 internal tide has a forcing frequency of $\omega_0 = 1.4 \times 10^{-4} \text{ rad} \cdot \text{s}^{-1}$, with typical horizontal wavelengths having an order of magnitude ~ 400 km ($k_h \sim 1.5 \times 10^{-5} \text{ m}^{-1}$) and horizontal phase speeds $2 \text{ m} \cdot \text{s}^{-1}$. We are free to choose the orientation θ from north of initial horizontal

wavenumber vector $(k_x, k_y) = (k_h \sin \theta, k_h \cos \theta)$.

The model is tested here for a constant buoyancy frequency of $\overline{N}_0^2 = 1 \times 10^{-4} \text{ s}^{-2}$. Through the dispersion relation (18), for a mode 1 wave at $y_0 \ll -W$ the resulting M2 horizontal wavelength is of order 600 km, a value on the larger side.

The wavepacket is initialized with inner oscillations of ω_0 fixed at the M2 forcing frequency (figure (4)). The effect of the rotation is included using $f = \beta y_0$. The envelope has a typical width of σ_x and σ_y with an amplitude fixed as $A_0 = 0.01 \times H$ with H the depth of the ocean previously used for computing the vertical modes. The wavepacket can be launched from different locations (x_0, y_0) and with various angles θ compared to the north.

The kinetic energy (KE), available potential energy (APE) and total energy (TE=KE+APE) of the different modes of the internal tides are computed numerically using the vertical mode decomposition:

$$\text{KE}_n = \frac{1}{2} \iint (u_n^2 + v_n^2) dx dy \int (\Phi_n^2)' dz, \quad (37)$$

$$\text{APE}_n = \frac{1}{2\overline{N}_0^2} \iint b_n^2 dx dy \int \overline{N}_0^2 \Phi_n^2 dz. \quad (38)$$

The total energy budget is also computed:

$$\partial_t(KE + APE) = -uv\partial_y U - uw\partial_z U - \frac{1}{\overline{N}^2}bv\partial_y B - \frac{1}{\overline{N}^2}bw\partial_z B, \quad (39)$$

where the two first terms of the right hand side correspond to shear production and the two others to buoyancy production.

4 Results for the model $\overline{N}_0 = \text{constant}$

4.1 No Equatorial jet

4.1.1 Trajectories and dynamics

The model is first tested without any equatorial jet, to check the propagation of the wavepacket and the influence of the rotation on its dynamics through the beta-plane approximation. In all that follows, the buoyancy frequency is kept constant, at $\overline{N}_0^2 = 1 \times 10^{-4} \text{ s}^{-2}$. In that case, (32), (34) and (35) reduce to decoupled equations for each mode:

$$\partial_t u_n - \beta y v_n - c_n^2 \partial_x b_n = 0, \quad (40a)$$

$$\partial_t v_n + \beta y u_n - c_n^2 \partial_y b_n = 0, \quad (40b)$$

$$\partial_t b_n - (\partial_x u_n + \partial_y v_n) = 0, \quad (40c)$$

where $c_n^2 = (\omega_0^2 - (\beta y)^2)/k_h^2$.

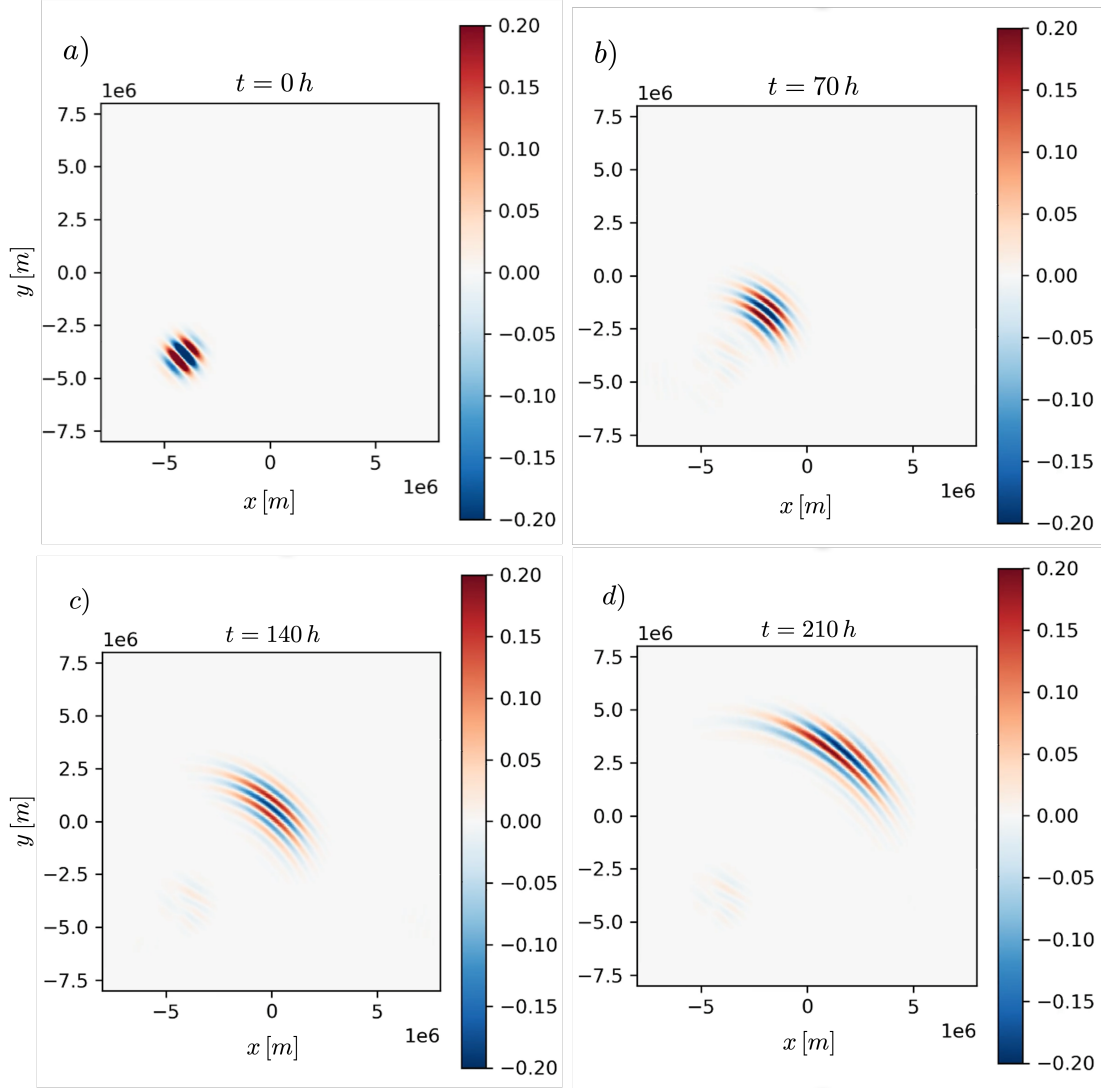


Figure 5: Zonal velocity ($\text{m}\cdot\text{s}^{-1}$) of vertical mode 1 M2 internal tide. The wavepacket is launched from $(x_0, y_0) = (-0.5 L_x, -0.5 L_y)$ with $\theta = \pi/4$.

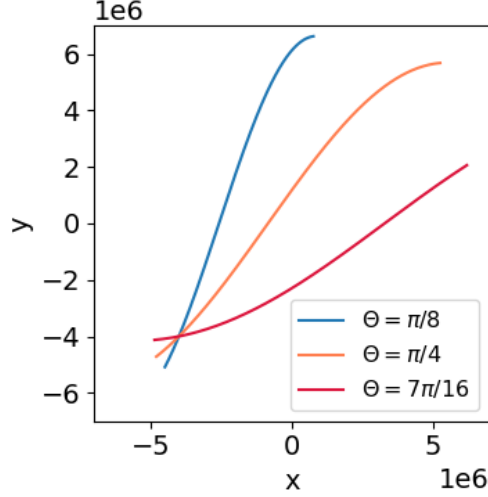


Figure 6: Trajectories computed using ray tracing for different angles of launch θ .

For a mode 1 wave ($n = 1$), c_1 is fixed. Setting $\omega_0 = 1.4 \times 10^{-4} \text{ rad.s}^{-1}$ yields the initial wavenumber $k_{h0} = 7.2 \times 10^{-6} \text{ m}^{-1}$.

Figure (5) shows the evolution of a wavepacket, launched from $(x_0, y_0) = (-Lx/2, -Ly/2) = (-4000, -4000) \text{ km}$ with an angle of $\theta = \pi/4$ and $\sigma_x = \sigma_y = 500 \text{ km}$. As such, the wavepacket is quasi-monochromatic, with $\sigma k_{h0} \gg 1$. As it crosses the domain, its trajectory slightly deviated. It is also subjected to significant dispersion due to the limited number of wavelengths composing it. The measurements over time in simulations yield values around $c_p = 27 \text{ m.s}^{-1}$ and $c_g = 9 \text{ m.s}^{-1}$ for the mode 1.

4.1.2 Ray tracing

The ray tracing analysis (see section 2.5 with $\omega_{\text{int}} = \omega_0$) can help disentangle the effect of the rotation over the wavepacket. In the β -plane approximation, the trajectory of the wavepacket can be computed using (28) with $E(y) = 0$:

$$x(y) = \frac{1}{\sqrt{C_1\beta^2}} \text{atan} \left(\frac{y}{\sqrt{C_2 - y^2}} \right), \quad (41)$$

with:

$$C_1 = \frac{\pi^2}{H^2 k_{x0}^2 (\overline{N}_0^2 - \omega_0^2)}, \quad \text{and} \quad C_2 = \frac{1}{\beta^2} \left(\omega_0^2 - \frac{1}{C_1} \right) \quad (42)$$

This expression is valid provided:

$$y^2 < C_2 = \frac{\omega_0^2}{\beta^2} - \frac{1}{C_1\beta^2} \quad (43)$$

The effect of the rotation and the influence of the initial angle of launch both directly influence the trajectory of the wavepacket through (41).

Figure (6) shows the expected trajectories for angles of $\theta = \pi/4$, $\theta = \pi/8$ and $\theta = 7\pi/16$. Rotation is responsible for the observed deviation of the trajectories. This effect also tends to disappear as the wavepacket approaches and crosses the Equator (where βy goes to zero).

Figure (7) shows the superposition of the computed trajectory with an initial angle of $\theta = 7\pi/16$ and the simulation. Both are in good agreement and illustrate how ray tracing succeeds in predicting the path of the wavepacket due to the rotation.

4.1.3 Energetics

In addition to the numerical computation (37), KE was computed analytically:

$$\text{KE}_1 = \frac{\pi}{16} A_0^2 \sigma_x \sigma_y \left(\overline{N}^2 + 2 \frac{m_1^2}{k_h^2} (\beta y)^2 \right), \quad (44)$$

Equation (44) shows how rotation directly acts as a source term of kinetic energy for internal tides.

Figure (8) shows the total energy (TE; left panel), kinetic energy (KE; middle panel) and available potential energy (APE; right panel) of the first mode of the internal tide corresponding to the case in figure (5). As only the first mode is initialized and because there is no jet to create new modes, all the wave energy is present in the first mode. The steady decrease of total energy (figure (8), left panel) is explained by the dissipation added to guarantee numerical stability (fixed at $\nu = 1 \text{ m}\cdot\text{s}^{-2}$). Over the time of the simulation, the loss of energy due to viscosity is $\sim 1\%$ initial energy. The kinetic energy (figure (8), middle panel) first decreases as the wavepacket approaches the Equator as a result of the term due to rotation in (44) tending to zero. Once the tide has crossed the Equator, the effect of rotation increases and KE increases again. APE (figure (8), right panel) changes as KE changes to keep the total energy nearly constant. In particular, at the Equator (here at $t \sim 90\text{h}$), equipartition of the energy between KE and APE is reached.

4.2 Vertically uniform equatorial jet

4.2.1 Jet configuration and M2 dynamics

The equatorial jet is added, centered on $y = 0$ with a characteristic width of $W = 400 \text{ km}$ and is uniform in the vertical:

$$U = U_0 \exp \left(-\frac{y^2}{2W^2} \right). \quad (45)$$

The strength of the jet and its direction is fixed by the value taken for U_0 (positive eastward and negative westward).

Following (45), the equations (32), (34) and (35) become:

$$\partial_t u_n + EU_0 \partial_x u_n + v_n E' U_0 - \beta y v_n - c_n^2 \partial_x b_n = 0, \quad (46a)$$

$$\partial_t v_n + EU_0 \partial_x v_n + \beta y u_n - c_n^2 \partial_y b_n = 0, \quad (46b)$$

$$\partial_t b_n + EU_0 \partial_x b_n - (\partial_x u_n + \partial_y v_n) = 0. \quad (46c)$$

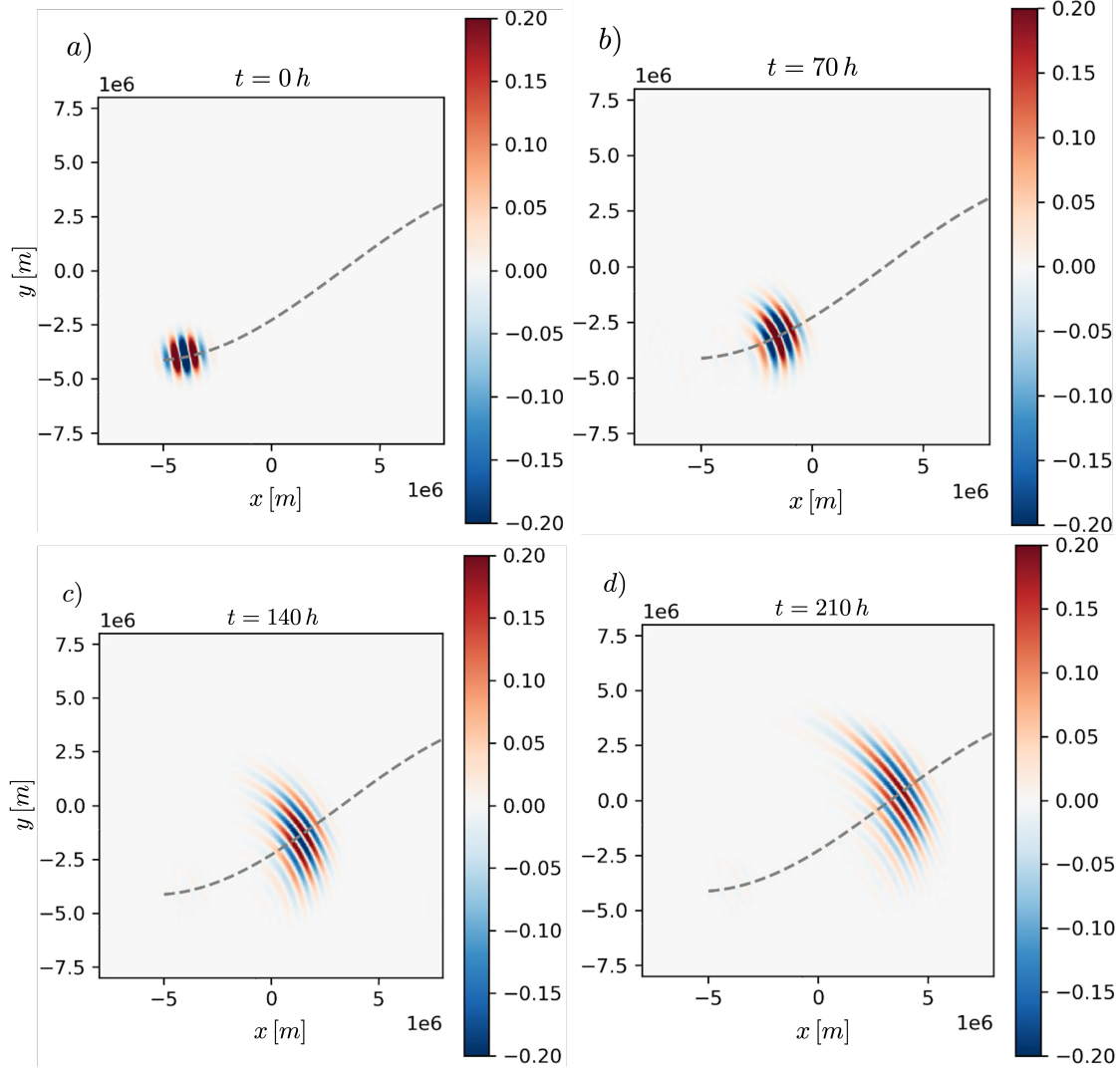


Figure 7: Colors: zonal velocity ($\text{m}\cdot\text{s}^{-1}$) of vertical mode 1 M2 internal tide. The wavepacket is launched from $(x_0, y_0) = (-0.5 L_x, -0.5 L_y)$ with $\theta = 7\pi/16$. Grey dashed lines: trajectory computed using ray tracing.

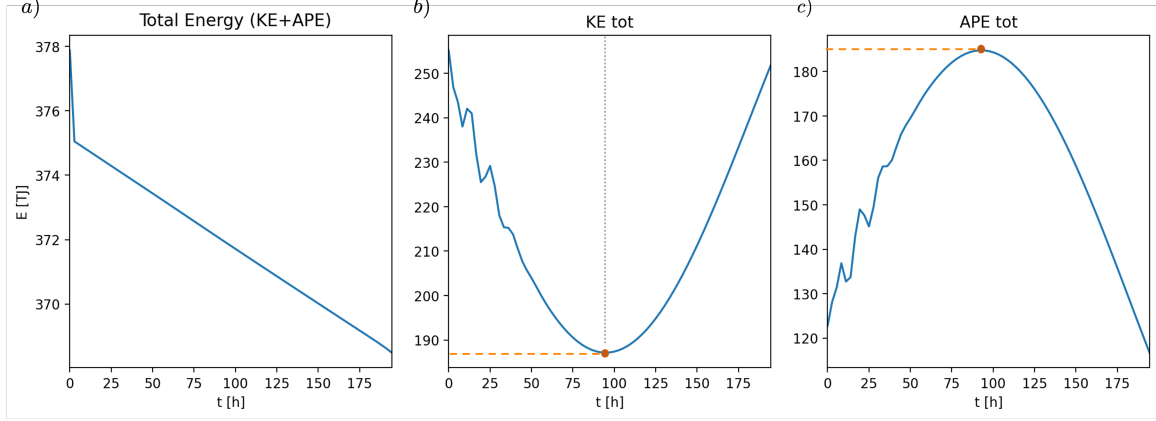


Figure 8: a) total energy, b) kinetic energy, c) available potential energy; all computed for the simulation presented in figure (5).

Again the lack of vertical structure to U decouples the mode-mode interactions. The added terms show that the flow mostly contributes to the advection of the wave. Only the term $v_n E' U_0$ in (46a) contributes to the interaction between the perturbations and the mean flow gradient.

4.2.2 Ray tracing

The trajectories of the wavepacket can be predicted with ray tracing (see section 2.5, with $\omega_0 = \omega_{\text{int}} + U k_x$). As the jet is located at the equator, where the rotation through the β -plane approximation is negligible, the Coriolis force is not included; $\omega_0 = \omega_{\text{int}}(k_x, k_y) + U k_x$ with $\omega_{\text{int}}(k_x, k_y)$ the dispersion relation (18), which is then independent of y . Using (28), we find

$$x(y) = k_{x_0} \left(\frac{c g x_{\text{int}}}{c g y_{\text{int}}} y + \frac{1}{c g y_{\text{int}}} \sqrt{\frac{\pi}{2}} W \operatorname{erf} \left(\frac{y}{\sqrt{2} W} \right) \right) \quad (47)$$

The trajectories for two jets of opposite direction ($U_0 = -5 \text{ m}\cdot\text{s}^{-1}$ and $U_0 = 5 \text{ m}\cdot\text{s}^{-1}$) are shown in figure (9). These results are valid only inside the jet, where the effect of the rotation is negligible. Depending on the direction of the jet and its intensity, the trajectory of the wavepacket is diverted in the direction opposite (case $U_0 = -5$) or toward ($U_0 = 5$) the direction propagation.

Figures (10) and (11) show two cases where the initial point of the wavepacket and its angle of launch ($(x_0, y_0) = (-7L_x/8, -L_y/2)$ and $\theta = 7\pi/16$) have been optimized to maximize the interactions with the jet. The jet is also stronger in both cases to enhance the effect. For a jet of $U_0 = -6 \text{ m}\cdot\text{s}^{-1}$ (figure 10), the crests are strongly diverted in the direction of the current. When approaching this level, the increase in k_y (smaller meridional wavelength) means the simulation under-resolves the waves. Conversely, for $U_0 = 6 \text{ m}\cdot\text{s}^{-1}$ (figure 11), the wavepacket largely reflects.

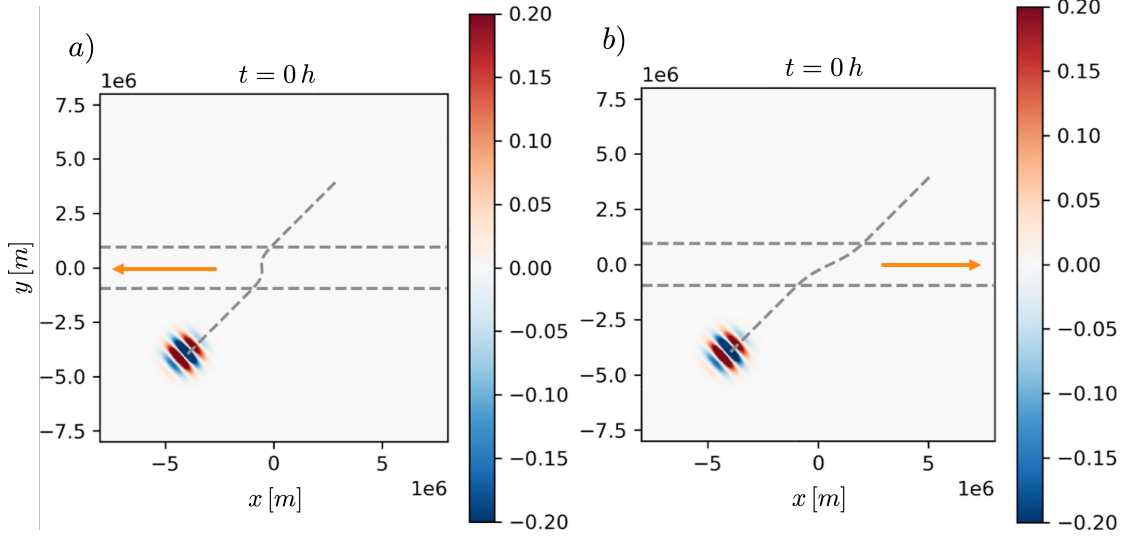


Figure 9: Zonal velocity ($\text{m}\cdot\text{s}^{-1}$) of vertical mode 1 M2 internal tide. The wavepacket is launched from $(x_0, y_0) = (-0.5 L_x, -0.5 L_y)$ with $\theta = \pi/4$. Trajectory computed using ray tracing shown by oblique grey dashed lines. Jet limits are denoted by horizontal grey dashed lines. Jet is uniform on the vertical with maximum amplitude set at $U_0 = 5\text{m}\cdot\text{s}^{-1}$, its direction varies according to the orange arrow: a) westward and b) eastward.

4.2.3 Energetics

Figure (12) shows the total energy (TE; left panel), kinetic energy (KE; middle panel) and available potential energy (APE; right panel) of the mode 1 wavepacket with no jet as in figure (8), also with a simulation computed with an westward jet having $U_0 = -1\text{ m}\cdot\text{s}^{-1}$ (grey dashed profiles). Because in both cases the dynamics do not involve higher modes, the total wave energy is contained in mode 1.

The interaction between the jet and the wave causes the total energy of the wavepacket to rise significantly as it enters the jet (around $t \sim 60\text{h}$), but the process reverses before the wavepacket exits the jet (around $t \sim 160\text{h}$). This reversal of the energy transfer occurs after the wavepacket crosses the Equator at around $t \sim 95\text{ h}$.

As no evolution of the jet or feedback from the jet is included into the model, the total energy is not conserved (in addition to the effect of dissipation, as shown in figure (12a)). In such configuration, it is the wave action $\mathcal{A} = \text{TE}/\omega_{\text{int}}$ that is conserved, provided that there is a scale separation between the wave and the jet.

Outside of the jet, where $\omega_{\text{int}} = \omega_0$, TE is given by:

$$\text{TE} = \mathcal{A} \omega_0, \quad (48)$$

where ω_0 is fixed at the excitation frequency of the M2 internal tide and \mathcal{A} is affected by the dissipation, causing the initial decrease observed in figure (12a).

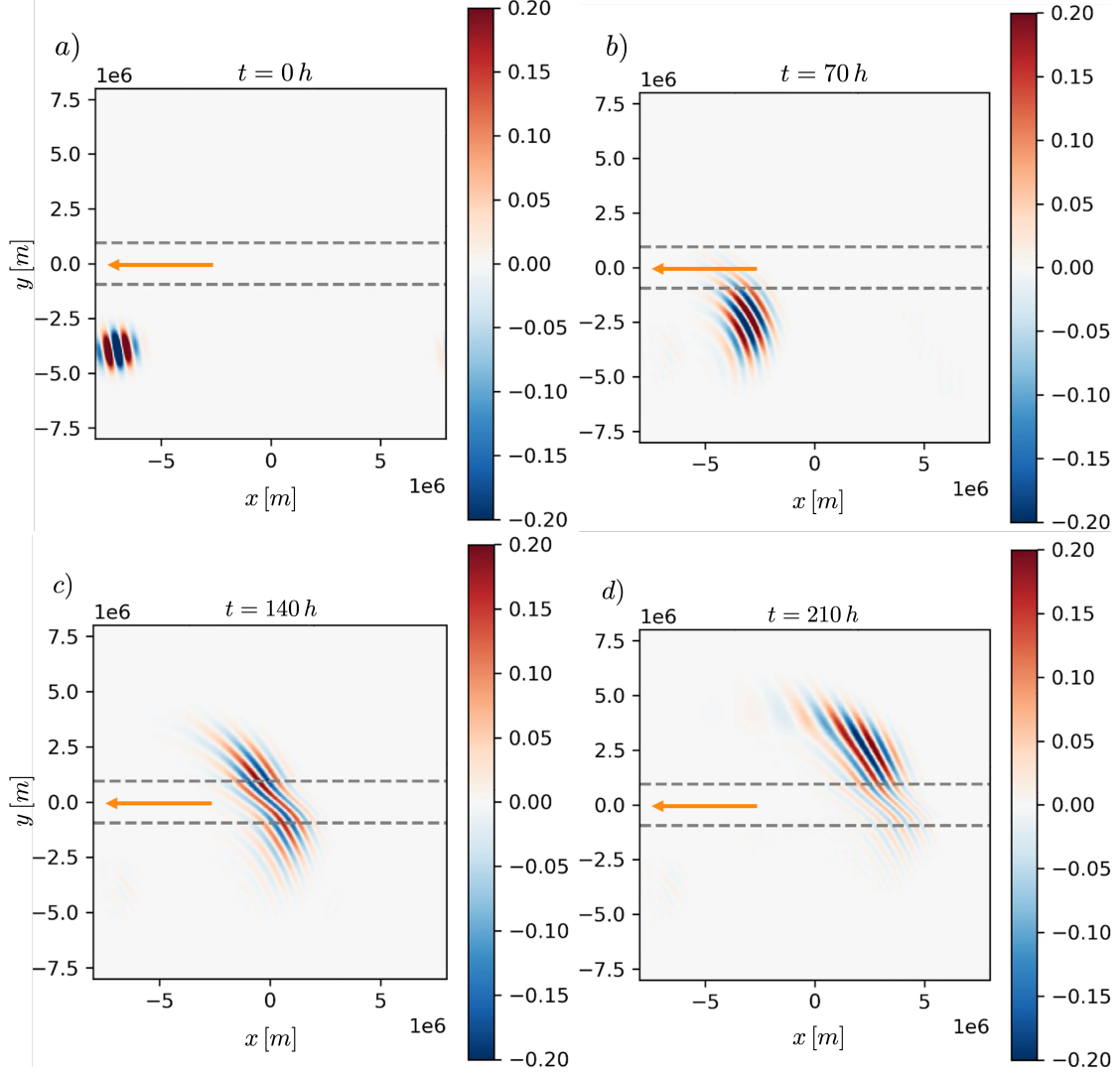


Figure 10: Zonal velocity ($\text{m}\cdot\text{s}^{-1}$) of vertical mode 1 M2 internal tide. The wavepacket is launched from $(x_0, y_0) = (-0.9 L_x, -0.5 L_y)$ with $\theta = 7\pi/16$. Jet limits are denoted by horizontal grey dashed lines, its direction by the orange arrow. Jet is uniform on the vertical with $U_0 = -6\text{m}\cdot\text{s}^{-1}$.

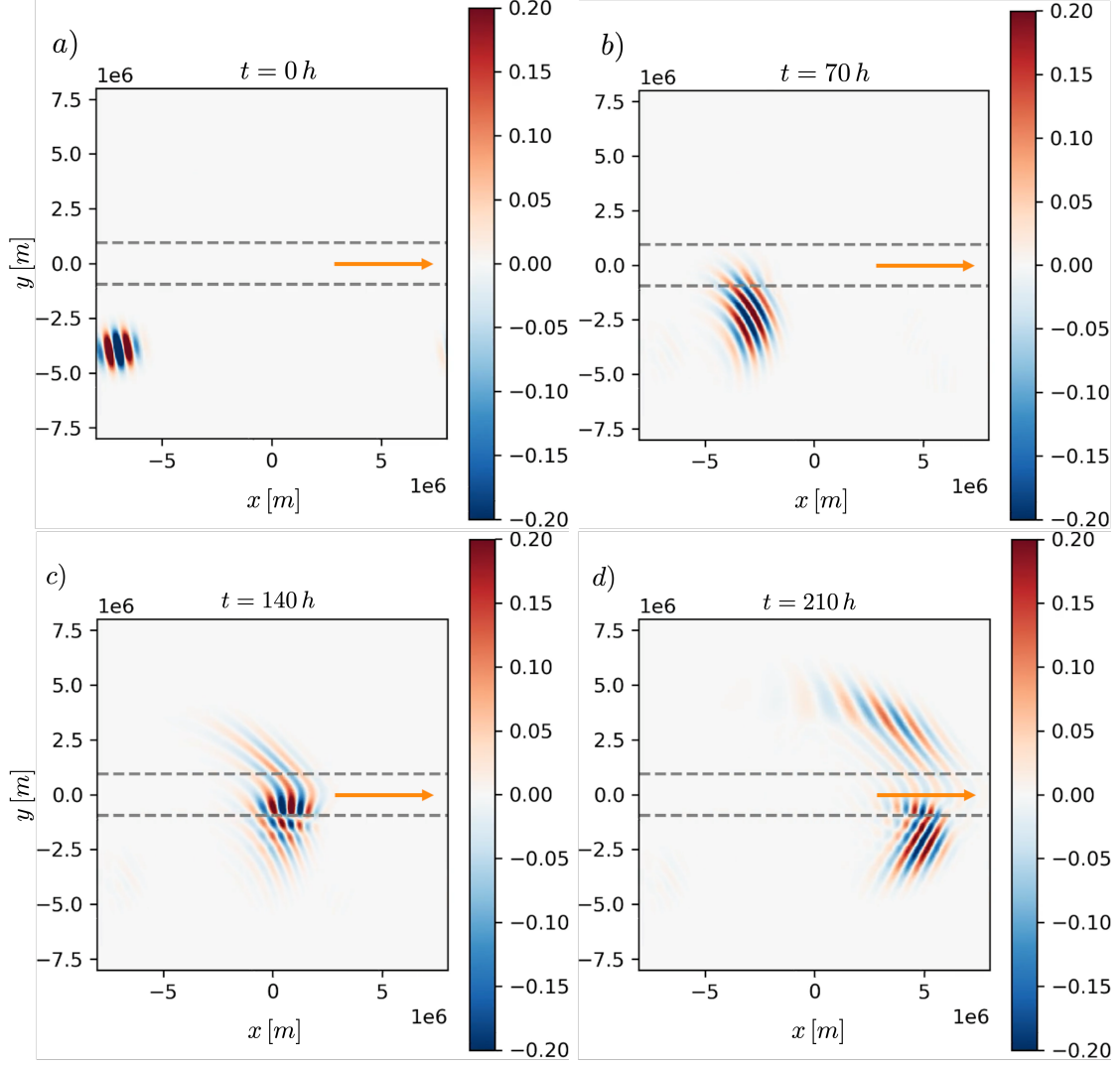


Figure 11: Zonal velocity ($\text{m}\cdot\text{s}^{-1}$) of vertical mode 1 M2 internal tide. The wavepacket is launched from $(x_0, y_0) = (-0.9 L_x, -0.5 L_y)$ with $\theta = 7\pi/16$. Jet limits are denoted by horizontal grey dashed lines, its direction by the orange arrow. Jet is uniform on the vertical with $U_0 = 6\text{m}\cdot\text{s}^{-1}$.

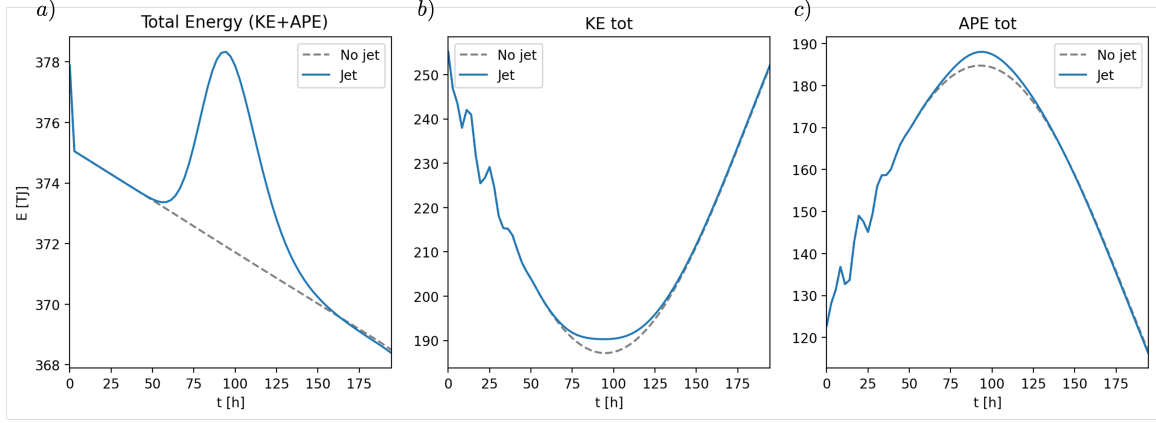


Figure 12: a) total energy, b) kinetic energy, c) available potential energy. Blue profiles correspond to the case with no jet, grey dashed lines for the jet uniform on the vertical with amplitude $U_0 = -1 \text{ m}\cdot\text{s}^{-1}$.

Inside the jet $\omega_{\text{int}} = \omega_0 - E(y)k_{x0}$. With $E(y) < 0$ as is the case in figure (12), ω_{int} increases to a maximum before decreasing back to ω_0 as the wavepacket exits the jet. As

$$\text{TE} = \mathcal{A}(\omega_0 - E(y)k_{x0}), \quad (49)$$

it means that, superimposed to the steady decrease caused by dissipation, TE first increases to a maximum due to wave/jet interactions before decreasing back to the value imposed by the dissipation when the wavepacket exits the jet.

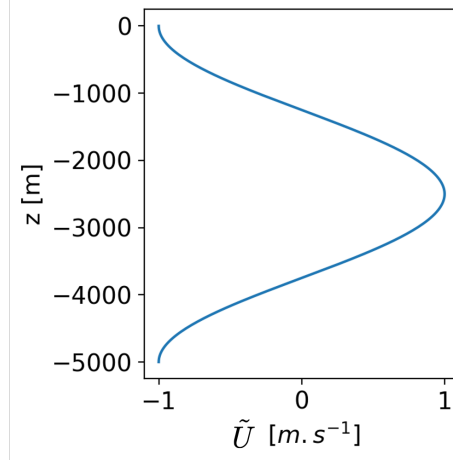


Figure 13: Vertical structure \tilde{U} of the jet as described in (50).

4.3 Vertical mode 2 Equatorial jet

4.3.1 Jet configuration and M2 dynamics

The horizontal structure of the Equatorial jet is kept identical but its vertical structure corresponds to a vertical mode 2 ($n = 2$):

$$U(y, z) = U_0 \cos(m_n z) \exp\left(-\frac{y^2}{2W^2}\right), \quad (50)$$

where $m_n = 2\pi/H$, $U_0 = -1 \text{ m}\cdot\text{s}^{-1}$, $W = 400 \text{ km}$ and $H = 5 \text{ km}$.

The sheared vertical structure of the jet is displayed in figure (13) and represents an idealised Equatorial jet: westward at the top and bottom of the ocean but eastward in the center of the ocean.

With the jet sheared in the vertical, the model is driven by the modal equations (32), (34), (35) with non-trivial interactions coefficients. Equations (33) and (36) also become non-trivial, representing the interactions between the vertical modes of the waves. In particular, for a jet with a vertical mode 2 structure, the coefficients have non-zero values for the wave modes $m = n - 2$ and $m = n + 2$, except for the case $n = 1$ which has also a non-zero interaction coefficient with itself ($m = n = 1$).

Despite this, the evolution of the vertical mode 1 M2 internal tide is qualitatively similar to the cases with no jet or with a vertically uniform jet. For example, the evolution shown in figure (14) should be compared with figure (7) that has no jet.

Higher modes are excited, but at much smaller amplitudes than mode 1. Figure (15) shows how, the mode 1 wavepacket, when propagating inside the jet, generates mode 3 with smaller amplitude less than 10% that of the mode 1 wave. This higher mode propagates inside the jet, in the same direction as the incident wave. It eventually decays, giving its energy back

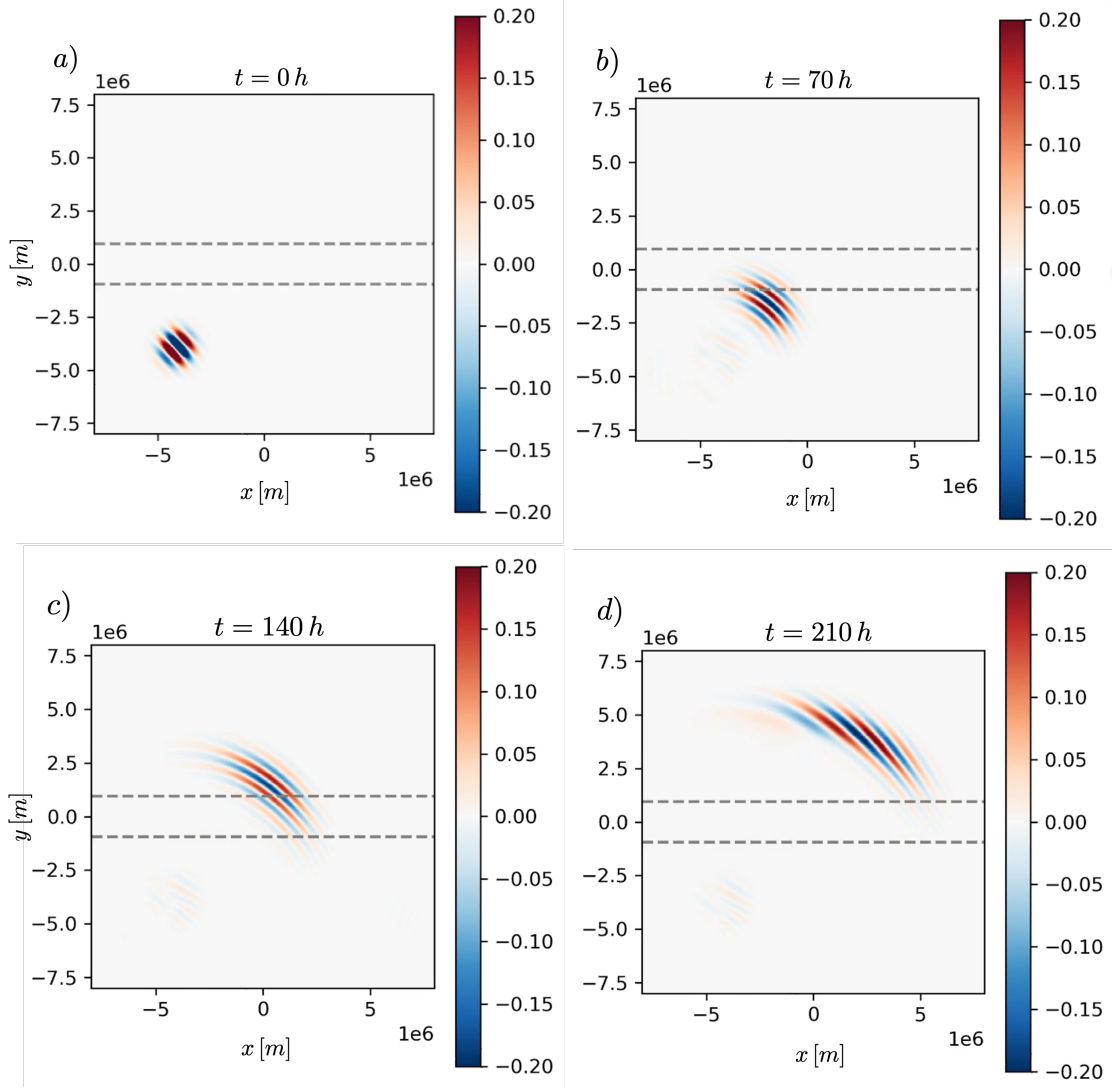


Figure 14: Zonal velocity ($\text{m}\cdot\text{s}^{-1}$) of vertical mode 1 M2 internal tide. The wavepacket is launched from $(x_0, y_0) = (-0.5 L_x, -0.5 L_y)$ with $\theta = \pi/4$. Jet limits are denoted by horizontal grey dashed lines, with a structure as in (50).

to mode 1 as the mode 1 leaves the jet. Such behaviour is also observed with higher modes, modes 5, 7, 9,..., all created inside the jet with smaller and smaller amplitudes and vanishing as the mode 1 wavepacket leaves the jet.

For the case treated here (where N is constant) and near the equator where $\beta|y| \sim 0$, the phase and group speeds are inversely proportional to the mode number. As a result, the wavepacket envelope as well as the crests of higher modes are slower than those of the initial mode 1. For example, for $\theta = \pi/4$, the mode 1 velocities are $c_{p1} = 27\text{m}\cdot\text{s}^{-1}$ and $c_{g1} = 9\text{m}\cdot\text{s}^{-1}$, whereas the mode 3 has $c_{p3} = 9\text{m}\cdot\text{s}^{-1}$ and $c_{g3} = 3\text{m}\cdot\text{s}^{-1}$.

These higher modes also have smaller horizontal wavelengths (the wavenumbers grow with the mode number), which would cause them to be more susceptible to dissipation and encountering critical layers. Numerically it means that the number of modes solved for is limited (to 10 in our case) as well as the maximum velocity of the jet.

4.3.2 Energetics

Figure (16) shows the total energy of the wavepacket (left panel) for the case with the mode 2 jet, first for all the vertical modes (dark blue profile), then for the mode 1 only (light blue profile). The case with no jet has also been added (grey dashed line). Compared to the variation caused by the wave-mean flow interaction, the difference brought by the creation of the higher modes is small. However, looking at the middle panel figure (16) that represents the difference between the total energy of all the modes and that of mode 1, shows that this difference still accounts for more than 200 MJ and develops only when the M2 internal waves crosses the jet. In the right panel of figure (16), this difference in the total energy is mostly explained when also adding the total energies of mode 3 and mode 5. As such, it shows how the higher modes created inside the jet are the result of the scattering of the energy from mode 1 to the modes of higher order, made possible by the interaction with the jet's non-uniform vertical structure.

The difference between the total energy and the energy of the mode 1, due to the scattering of energy to higher modes, is observed to decay at later times, when the wavepacket exits the jet, it corresponds to the vanishing of the higher modes signal observed in figure (15). This scattered energy is returned to the mode 1, as observed for the energy of the wave-mean flow interaction in figure (12). Also, successive higher modes created receive less and less energy, as their amplitudes decrease with mode number.

The left panel of figure (17) shows the total energy of the mode three, which is the first to be created through wave-mean flow interactions and also the higher mode that receives the most energy. The comparison with the case without the jet is added in grey dashed lines to show how the creation is only possible with the addition of the vertically mode 2 jet. The middle panel of figure (17) presents only the kinetic energy of the mode 3. It demonstrates how the scattering of energy to the higher modes is realised through the growth of kinetic energy as it nearly accounts for the all of the mode's energy in comparison to the previous panel. The right panel of figure (17) shows the kinetic energy of all the higher

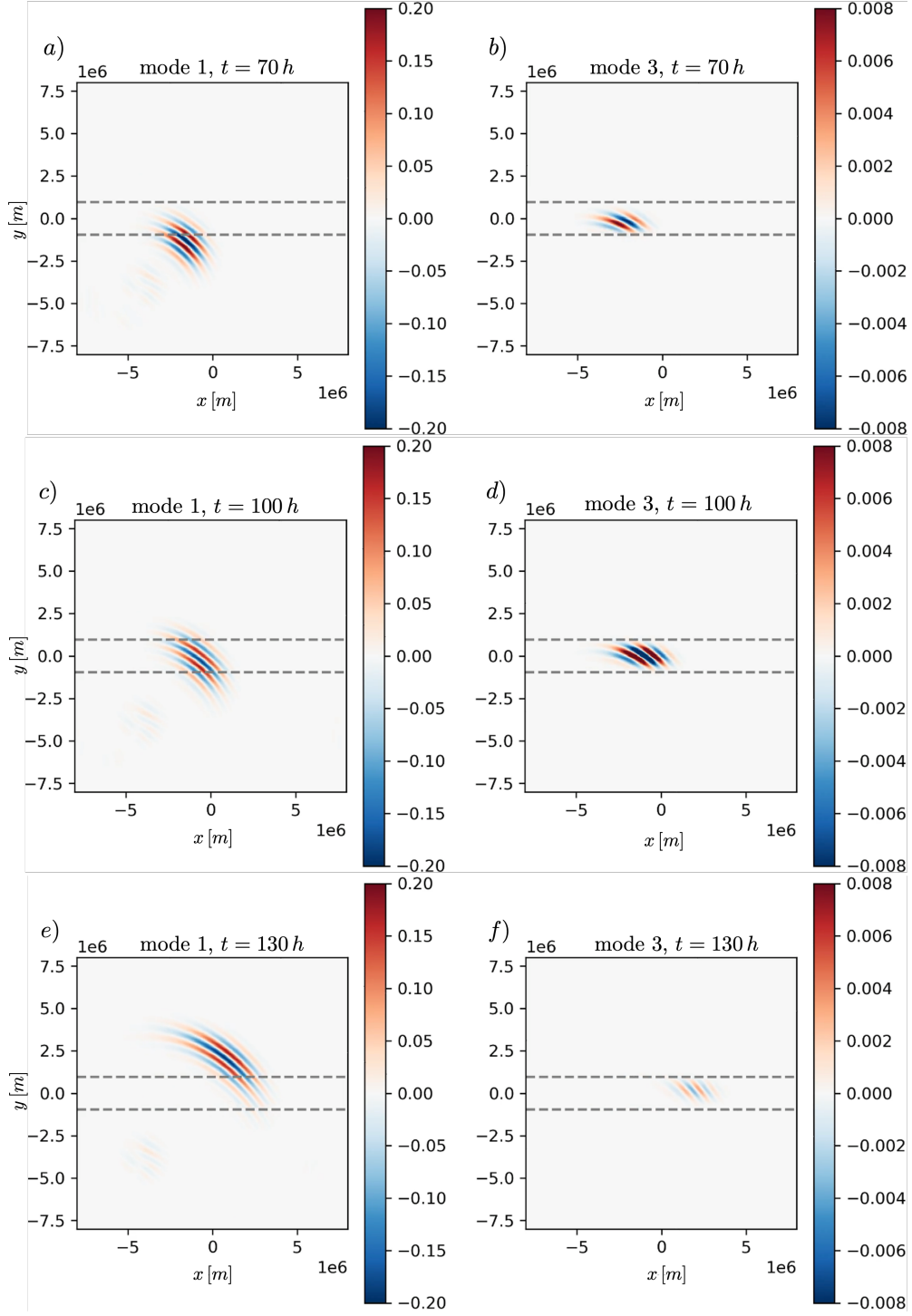


Figure 15: Zonal velocity ($\text{m}\cdot\text{s}^{-1}$) of vertical mode 1 (panels a), c), e)) and mode 3 (panels b), d), f)) M2 internal tide. The wavepacket is launched from $(x_0, y_0) = (-0.5 L_x, -0.5 L_y)$ with $\theta = \pi/4$. Jet limits are denoted in grey dashed lines, with a structure as in (50).

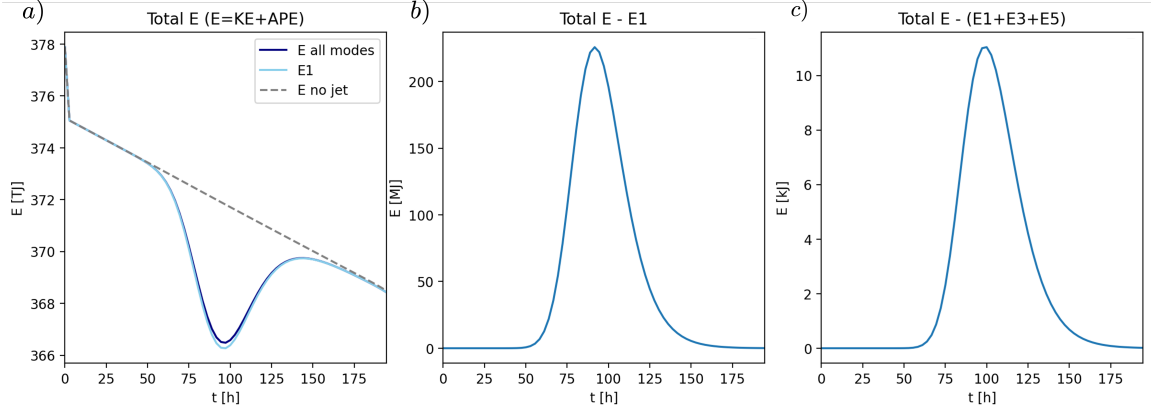


Figure 16: a) total energy. Grey dashed profile corresponds to the case with no jet, light blue to the total energy of mode 1 with the sheared jet and darker blue to the total energy of all the modes combined, in the case of the sheared jet. b) difference between the total energy in the domain and the total energy of the mode 1. c) difference between the total energy in the domain and the total energy of the modes 1, 3 and 5 combined.

modes created (the maximum number of vertical modes solved for here is 10), normalised by their maximum value. It shows how the modes are created subsequently, mode 3 then mode 5, 7 and 9. The reverse transfer of energy toward mode 1 then occurs in the inverse order, mode 9 being the first to give all its energy back to mode 7 then mode 7 to mode 5 and so forth to mode 1. This effect is somewhat masked by the normalisation (right panel of figure (17)) as it shows that mode 9 seems to be the last to vanish. However, mode 9 represents so little energy compared to mode 3, that the tail of the distribution of mode 3 (around $t \sim 160$) still contains more of the total energy than what is distributed amongst the higher modes. The last mode to transfer its energy to mode 1 is then effectively mode 3.

Figure (18) shows the evolution of each term of the energy budget (39). The dominant terms are those of shear production (blue and orange profiles), related to the horizontal and vertical shear of the mean flow. Both shear contributions change sign after the wavepacket crosses the Equator. The part due to the vertical shear of the mean flow constitutes the biggest contribution to the energy budget as the shear is more intense being localised over the 5 km depth, as opposed to the 400 km of width the Equatorial jet. The terms of buoyancy production do not contribute to the evolution of the total energy.

4.3.3 Possible incoherence?

Coming back to the motivating question, we want to check if the wave-mean flow interaction could explain the lack of observed M2 internal tide signal in the Equatorial Pacific [1].

We found the overall propagation of the tidal mode 1 negligibly changes with or without a sheared jet (figure (5) and (14)) and the processes related to the excitation of higher modes reverse when the wavepacket exits the jet (see section 4.3). To check if there are any differences due to the interaction with and without a jet, we assess wave incoherence, from

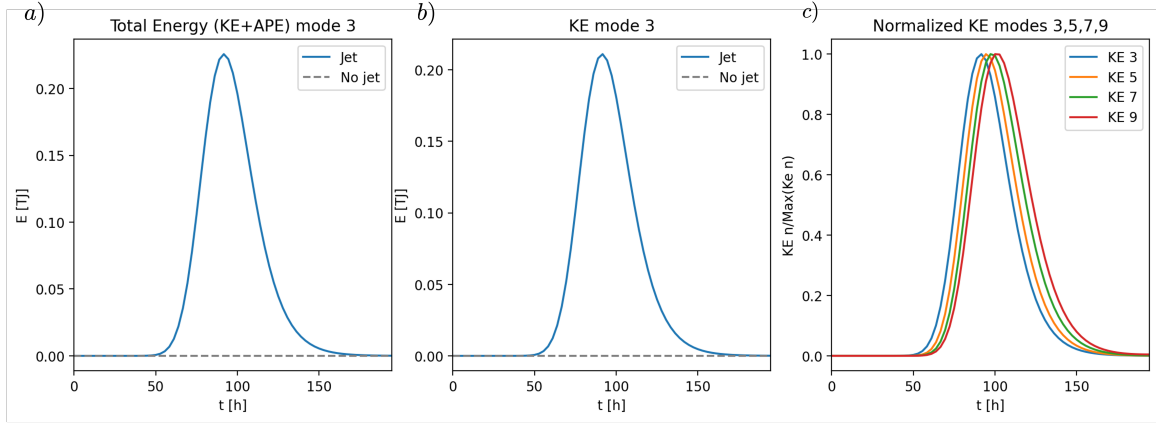


Figure 17: a) total energy of mode 3. Grey dashed profile corresponds to the case with no jet and blue profile to the sheared jet case. b) kinetic energy of mode 3. c) kinetic energy of modes 3 (blue), 5 (orange), 7 (green) and 9 (red), normalized by their maximum values respectively.

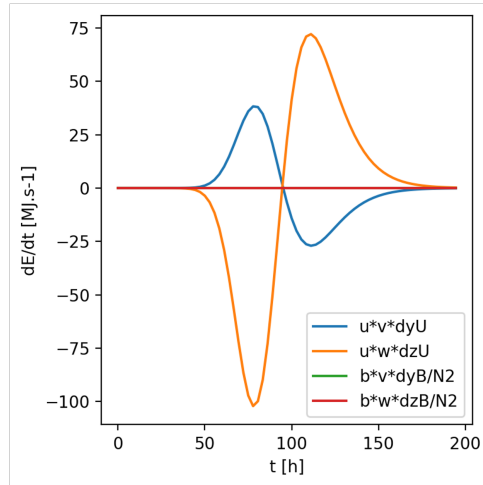


Figure 18: Variation of the different terms of the energy budget, as computed in (39).

the difference between the case with the mode 2 jet and the case with no jet.

Figure (19) shows how a difference in the dynamics is indeed created by the addition of the sheared jet. The difference only becomes significant when the wavepacket enters the jet and grows as long as both interact. The difference remains after the wavepacket is well north of the jet. This is unlike the dynamics and energy transfer observed for the creation of higher modes and it points toward the creation of lasting incoherence due to the wave-mean flow interaction.

Figure (20) is a schematic representation of our interpretation of such incoherence. As the mode 1 wavepacket enters the vertically sheared jet, energy is scattered toward higher modes. These modes propagate at a speed that is lower than that of mode 1 (both the group and phase speed are lower the higher the mode number). When the reverse transfer of energy occurs as the wavepacket propagates north of the Equator, the energy is transferred back to mode 1, but with a shift caused by the difference of phase speeds. The mode 1 wavepacket thus becomes phase shifted, creating incoherence in the internal tide signal. This incoherence is a possible explanation of the lack of internal tide signal detected north of the equator in the Equatorial Pacific [1].

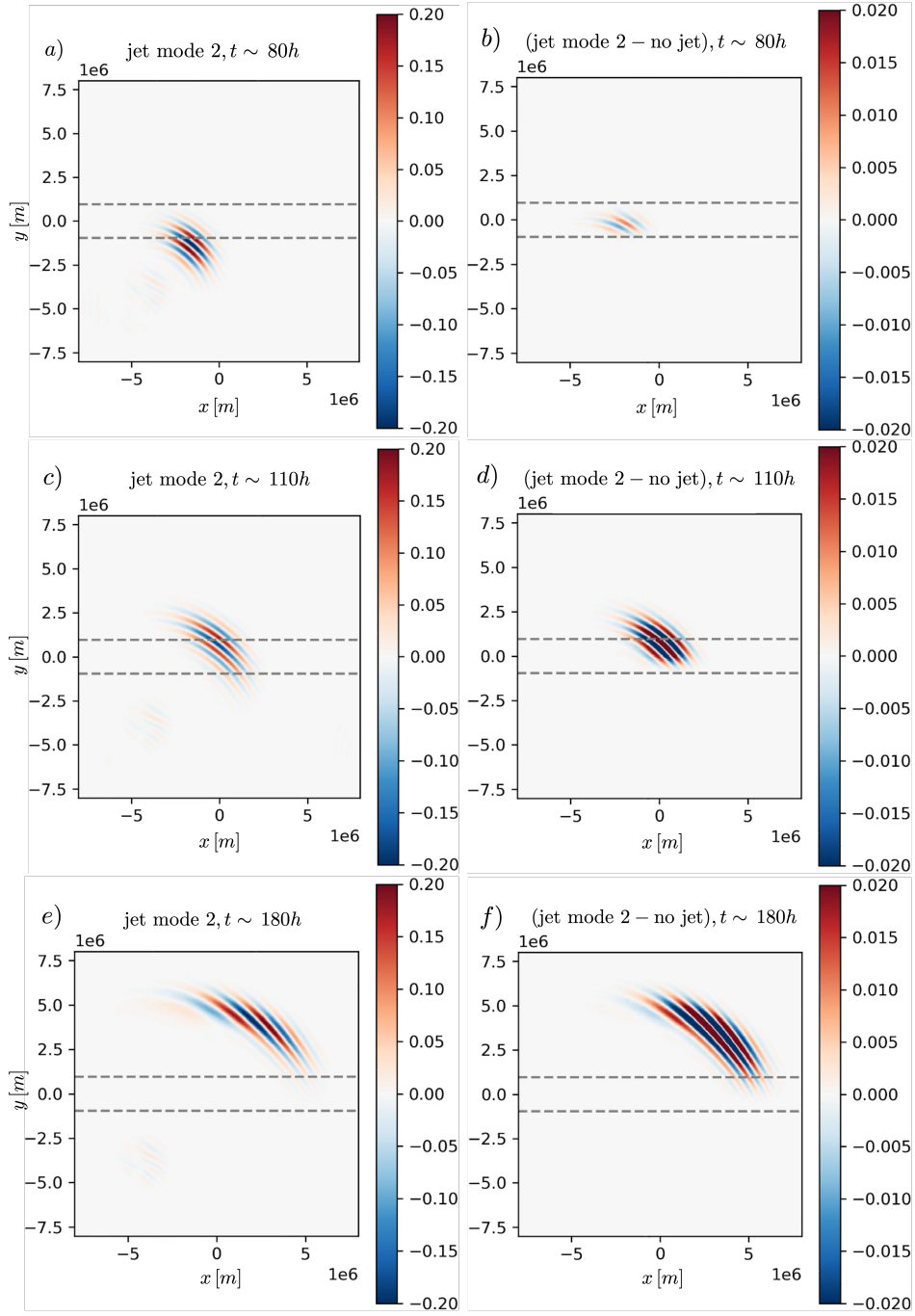


Figure 19: Zonal velocity ($\text{m}\cdot\text{s}^{-1}$) of vertical mode 1 M2 internal tide with the sheared mode 2 jet (panels a), c), e)). Difference in the zonal velocity of vertical mode 1 M2 internal tide between the case with the sheared jet and the case with no jet (panels b), d), f)). The wavepacket is launched from $(x_0, y_0) = (-0.5L_x, -0.5L_y)$ with $\theta = \pi/4$. Jet limits are denoted in grey dashed lines, with a structure as in (50).

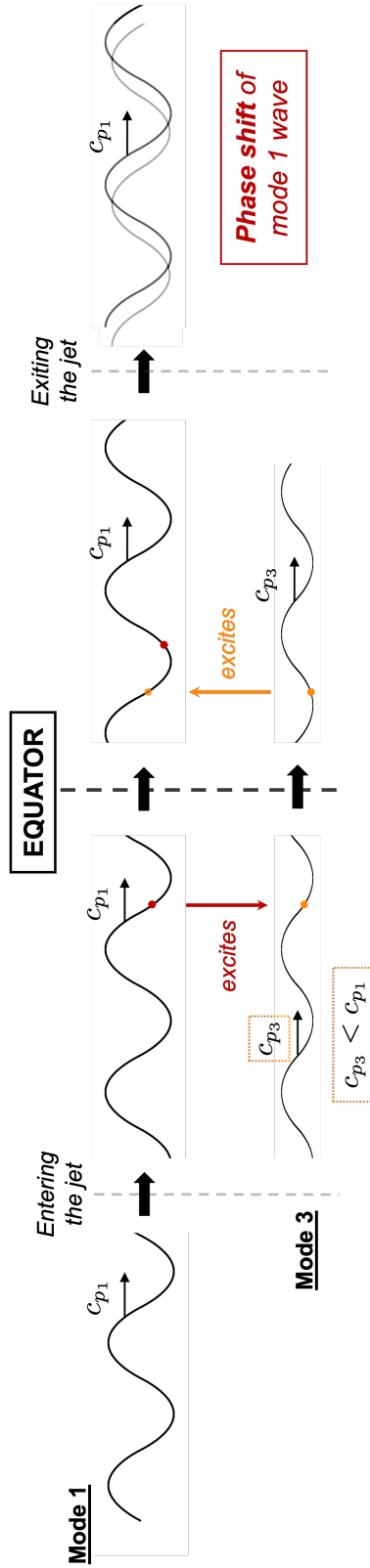


Figure 20: Scheme of the incoherence mechanisms due to wave-mean flow interaction and the creation of higher modes.

5 Conclusion

We have investigated, by means of theory and numerical simulations within a idealised setup, the wave-mean flow interaction between a mode 1 M2 internal tide and a vertically uniform and sheared equatorial jet. The aim was to validate if such interactions could result in incoherence and hence explain the lack of M2 altimetry signal in the Equatorial Pacific.

We have identified different effects that can influence the dynamics of the M2 wavepacket. The β -effect deflects the path of the wavepacket but has negligible influence immediately at the Equator. A vertically uniform jet could, depending on its strength, lead to total reflection of the wavepacket or strong distortion of the crests. A vertically sheared jet however scatters energy to higher modes. These higher modes have smaller horizontal wavelength but also lower phase and group speed. The transfer of energy is reversed after the wavepacket crosses the Equator, the higher modes vanishing and all the energy going back into mode 1. It is the difference of propagation speed between the different modes that could explain the creation of incoherence in the signal, that would affect the altimetry observations [1].

Because of their smaller horizontal wavelength and lower phase and group speed, the higher modes excited by the jet are likely to be more sensitive to dissipation, but also to critical layers in a case where N is not constant. It could cause further deposition of energy inside the jet and hence modify its dynamics as well as that of the wavepacket. It is an effect that we will develop further in future work.

The theoretical tools developed here are readily adapted to realistic profiles of stratification and equatorial currents. In particular, future work will model stratification motivated by observations and a zonal equatorial jet with strong westward near-surface flow and underlying countercurrents, as shown in figure (1).

6 Acknowledgements

I sincerely thank Bruce Sutherland and Lois Baker who supervised this project and from whom I learned a lot during this summer. They showed great patience and unwavering support at every step of the way, for which I am extremely grateful. I also want to deeply thank Keaton Burn and Eric Ester for the precious help they provided regarding Dedalus and how to build a numerical model from scratch. At last, I wish to profoundly thank everyone that was at Walsh Cottage this summer and who made this experience so wonderful and enriching.

References

- [1] Buijsman, M. C., B. K. Arbic, J. G. Richman, J. F. Shriver, A. J. Wallcraft, and L. Zamudio, “Semidiurnal internal tide incoherence in the equatorial Pacific”, *J. Geophys. Res. (Oceans)*, **122**(7), 5286–5305, 2017, doi:10.1002/2016JC012590.
- [2] Ferrari, R., and C. Wunsch, “Ocean Circulation Kinetic Energy: Reservoirs, Sources, and Sinks”, *Annu. Rev. Fluid Mech.*, **41**(1), 253–282, 2009, doi:10.1146/annurev.fluid.40.111406.102139.
- [3] Martin, J. P., D. L. Rudnick, and R. Pinkel, “Spatially Broad Observations of Internal Waves in the Upper Ocean at the Hawaiian Ridge”, *J. Phys. Oceanogr.*, **36**(6), 1085, 2006, doi:10.1175/JPO2881.1.
- [4] MacKinnon, J. A., Z. Zhao, C. B. Whalen, A. F. Waterhouse, D. S. Trossman, O. M. Sun, L. C. St. Laurent, H. L. Simmons, K. Polzin, R. Pinkel, A. Pickering, N. J. Norton, J. D. Nash, R. Musgrave, L. M. Merchant, A. V. Melet, B. Mater, S. Legg, W. G. Large, E. Kunze, J. M. Klymak, M. Jochum, S. R. Jayne, R. W. Hallberg, S. M. Griffies, S. Diggs, G. Danabasoglu, E. P. Chassignet, M. C. Buijsman, F. O. Bryan, B. P. Briegleb, A. Barna, B. K. Arbic, J. K. Ansong, and M. H. Alford, “Climate Process Team on Internal Wave–Driven Ocean Mixing”, *Bull. Amer. Meteor. Soc.*, **98**(11), 2429–2454, 2017, doi:10.1175/BAMS-D-16-0030.1.
- [5] Sutherland, B. R., *Internal Gravity Waves*, Cambridge University Press, Cambridge, 2010.
- [6] Gerkema, T., and J. T. F. Zimmerman, “An introduction to internal waves”, in *Proceedings of ...*, 2008.
- [7] Kelly, S. M., “The Vertical Mode Decomposition of Surface and Internal Tides in the Presence of a Free Surface and Arbitrary Topography”, *J. Phys. Oceanogr.*, **46**(12), 3777–3788, 2016, doi:10.1175/JPO-D-16-0131.1.
- [8] Kelly, S. M., P. F. J. Lermusiaux, T. F. Duda, and P. J. Haley Jr., “A Coupled-Mode Shallow-Water Model for Tidal Analysis: Internal Tide Reflection and Refraction by the Gulf Stream”, *J. Phys. Oceanogr.*, **46**(12), 3661–3679, 2016, doi:10.1175/JPO-D-16-0018.1.
- [9] Kelly, S. M., and P. F. J. Lermusiaux, “Internal-tide interactions with the Gulf Stream and Middle Atlantic Bight shelfbreak front”, *J. Geophys. Res. (Oceans)*, **121**(8), 6271–6294, 2016, doi:10.1002/2016JC011639.
- [10] Garrett, C., and E. Kunze, “Internal Tide Generation in the Deep Ocean”, *Annu. Rev. Fluid Mech.*, **39**(1), 57–87, 2007, doi:10.1146/annurev.fluid.39.050905.110227.
- [11] Dunphy, M., and K. G. Lamb, “Focusing and vertical mode scattering of the first mode internal tide by mesoscale eddy interaction”, *J. Geophys. Res. (Oceans)*, **119**(1), 523–536, 2014, doi:10.1002/2013JC009293.

- [12] Kelly, S. M., A. F. Waterhouse, and A. C. Savage, “Global Dynamics of the Stationary M_2 Mode-1 Internal Tide”, *Geophys. Res. Lett.*, **48**(11), e91692, 2021, doi:10.1029/2020GL091692.
- [13] Sarkar, S., and A. Scotti, “From Topographic Internal Gravity Waves to Turbulence”, *Annu. Rev. Fluid Mech.*, **49**, 195–220, 2017, doi:10.1146/annurev-fluid-010816-060013.
- [14] Lamb, K. G., “Internal Wave Breaking and Dissipation Mechanisms on the Continental Slope/Shelf”, *Annu. Rev. Fluid Mech.*, **46**, 231–254, 2014, doi:10.1146/annurev-fluid-011212-140701.
- [15] Munk, W., and C. Wunsch, “Abyssal recipes II: energetics of tidal and wind mixing”, *Deep-Sea Res. Part I*, **45**(12), 1977–2010, 1998, doi:10.1016/S0967-0637(98)00070-3.
- [16] Rainville, L., and R. Pinkel, “Propagation of the low-modes internal waves through the ocean”, in *AGU Spring Meeting Abstracts*, **2004**, OS33B-05, 2004.
- [17] Burns, K. J., G. M. Vasil, J. S. Oishi, D. Lecoanet, and B. P. Brown, “Dedalus: A flexible framework for numerical simulations with spectral methods”, *Phys. Rev. Res.*, **2**(2), 023068, 2020, doi:10.1103/PhysRevResearch.2.023068.
- [18] de Lavergne, C., S. Falahat, G. Madec, F. Roquet, J. Nycander, and C. Vic, “Toward global maps of internal tide energy sinks”, *Ocean Modell.*, **137**, 52–75, 2019, doi:10.1016/j.ocemod.2019.03.010.
- [19] Marshall, J., A. Adcroft, C. Hill, L. Perelman, and C. Heisey, “A finite-volume, incompressible Navier Stokes model for studies of the ocean on parallel computers”, *J. Geophys. Res. (Oceans)*, **102**(C3), 5753–5766, 1997, doi:10.1029/96JC02775.